Brain Imaging and Behavior (2019) 13:699–716
https://doi.org/10.1007/s11682-018-9869-1

ORIGINAL RESEARCH

Amyloid causes intermittent network disruptions in cognitively intact older subjects

Susanne G. Mueller[1,2]

Published online: 16 May 2018

Abstract

Recent findings in AD models but also human patients suggest that amyloid can cause intermittent neuronal hyperactivity. The overall goal of this study was to use dynamic fMRI analysis combined with graph analysis to a) characterize the graph analytical signature of two types of intermittent hyperactivity (spike-like (spike) and hypersynchronus-like (synchron)) in simulated data and b) to attempt to identify one of these signatures in task-free fMRIs of cognitively intact subjects (CN) with or without increased brain amyloid. The toolbox simtb was used to generate 33 data sets with 2 short spike events, 33 with 2 synchron and 33 baseline data sets. A combination of sliding windows, hierarchical cluster analysis and graph analysis was used to characterize the spike and the synchron signature. Florbetapir-F18 PET and task-free 3 T fMRI was acquired in 49 CN (age = 70.7 ± 6.4). Processing the real data with the same approach as the simulated data identified phases whose graph analytical signature resembled that of the synchron signature in the simulated data. The duration of these phases was positively correlated with amyloid load ($r = 0.42$, $p < 0.05$) and negatively with memory performance ($r = -0.43$, $p < 0.05$). In conclusion, amyloid positivity is associated with intermittent hyperactivity that is caused by short phases of hypersynchronous activity. The negative association with memory performance suggests that these disturbances have the potential to interfere with cognitive processes and could lead to cognitive impairment if they become more frequent or more severe with increasing amyloid deposition.

Keywords Amyloid · Intermittent · Functional connectivity · Cognitively intact · Hyperactivity · Resting state fMRI

Introduction

Several recent task-free fMRI publications suggest that abnormal functional connectivity might be one of the earliest manifestations of amyloid positivity in cognitively intact subjects (for example, Sheline et al. 2010; Brier et al. 2014; Wang et al. 2013; Sperling et al. 2009; Jack et al. 2013; Steininger et al. 2014). It is usually assumed that these connectivity disturbances are stable over time but recent findings suggest that this assumption might not be entirely correct. Studies in animal models of Alzheimer's disease (AD) but also in patients suffering from familial AD for example found that high levels of amyloid and amyloid plaques can cause intermittent neuronal hyperactivity (Born 2015; Stargardt et al. 2015). The best documented type of hyperactivity are Intermittent epileptic discharges that occur in animal models after amyloid aggregation and can evolve in later stages into clinically manifest seizures (Vossel et al. 2013, Mucke and Selkoe 2012, Palop and Mucke 2010, Talantova et al. 2013, Busche et al. 2012, Greinberger et al. 2012, Palop et al. 2007; Sanchez et al. 2012). Only about 2% of the patients diagnosed with mild cognitive impairment (MCI) or dementia due to sporadic AD show overt epileptiform discharges during routine EEG recordings (Liedorp et al. 2009). However, with prolonged recordings that also include sleep phases it is possible to observe epileptiform activity in up to 60% of the MCI and in about 20% of the AD patients (Vossel et al. 2016). In addition to overt epileptiform discharges, recent findings in animal studies suggest that oligomeric amyloid can cause at least one other type of hyperactivity. This hyperactivity is characterized by abnormal neuronal firing patterns caused by a higher failure rate to transition into the relatively depolarized state due to an abnormal synchronization of the inputs from

✉ Susanne G. Mueller
susanne.mueller@ucsf.edu

[1] Center for Imaging of Neurodegenerative Diseases, Department of Veterans Affairs (DVA) Medical Center, VAMC, Clement Street 4150, San Francisco, CA 94121, USA

[2] Department of Radiology and Biomedical Imaging, University of California, San Francisco, CA, USA

the network of interacting neurons (Stern et al. 2004; Kellner et al. 2014). These disturbances have been shown to be associated with hyperexcitability and hypersynchrony at the wider network level (Shah et al. 2016). One of the most interesting characteristics is that they can already be observed before pathological amyloid plaque aggregation and also before the appearance of overt epileptiform activity (Stern et al. 2004; Kellner et al. 2014; Shah et al. 2016). It is tempting to speculate that this type of activity could be responsible for the intermittent focal and/or diffuse hyperactivity, e.g., transient focal or widespread slow activity, that is found in 20–45% of the routine visual EEGs (Stomrud et al. 2010, Liedorp et al. 2009 and 2010) and the abnormal synchronization seen in quantitative EEG analyses (Smailovic et al. 2017) in MCI and AD patients. Complex interictal epileptiform discharges as well as focal and diffuse hypersynchrony have been associated with impaired cognitive performance (Kleen et al. 2013; Smits et al. 2011) which raises the possibility that both types of intermittent neuronal hyperactivity could have a negative impact on cognition in the preclinical and clinical stages of AD.

The first goal of this study was to obtain evidence for the existence of amyloid associated intermittent hyperactivity in task-free fMRI of cognitively intact subjects with and without increased brain amyloid. The traditional type of task-free analysis is based on the average connectivity across the whole acquisition time. However, in diseases known or suspected to be associated with intermittent or paroxysmal activity, these events are likely to be cancelled out by the long phases of physiological activity or cause unspecific connectivity disturbances. Therefore, a sliding windows approach, one of the most common dynamic fMRI analysis techniques (Hutchison et al. 2013), combined with a cluster analysis to identify different activity states and graph analysis to describe them was used in this study to capture the episodes of intermittent hyperactivity. The second goal was to investigate the relationship between these hyperactivity episodes and amyloid plaque load and cognition. The third and last goal was to learn more about the nature of these hyperactivity episodes by comparing their graph analytical features with those seen in simulated resting state data in which short episodes of the two types of amyloid associated hyperactivity discussed in the previous paragraph, i.e., epileptiform and hypersynchrony, had been modeled.

Materials and methods

Population

A total of 51 elderly (60 years and older), cognitively intact subjects who were recruited from local Memory Clinics and the community with flyers and advertisements in local newspapers participated in this study. Exclusion criteria included any poorly controlled medical illness (untreated diabetes, hypertension, thyroid disease) and/or use of medication or recreational drugs that could affect brain function, a history of brain trauma, brain surgery or evidence for ischemic events (stroke but not white matter hyperintensities or small lacunes) and skull defects on the MRI. Normal cognitive functioning was assessed by a battery of standard tests. Mini Mental State Examination (MMSE) and Clinical Dementia Rating (CDR) were administered as a quick screening tool to identify potential MCI. The Wechsler Adult Intelligence Scale III (WAIS III, digit symbol, matrix reasoning) and the Delis-Kaplan Executive Function System (DKEF, trail making, verbal fluency, design fluency) were used to assess different aspects of global cognitive function. The California Verbal Learning Test II (CVLT-II) was used to assess memory performance. From this battery, three CVLT-II subtests, Immediate Recall Discriminability, Short Free Discriminability and Delayed Recall Discriminability, were chosen to assess the impact of amyloid-associated hyperactivity on cognitive function because an association between these measures and brain structure had been in a previous study in this cohort (Mueller et al. 2011). Subjects were considered to be cognitively intact if they had a MMSE > 26 and a CDR = 0.0 and if they scored within 1.5 SD on all other tests. All participants underwent structural and functional imaging on a 3 T MRI and a florbetapir F18 (Amyvid ™) PET exam to determine the amyloid beta plaque load. Two patients had imaging data of insufficient quality and thus had to be excluded from the analysis, so that the final study population encompassed 49 subjects (please see Table 1 for demographic details of the final study population). The study was approved by the committees of human research at the University of California, San Francisco (UCSF) and VA Medical Center San Francisco, and written informed consent was obtained from all subjects according to the Declaration of Helsinki.

PET

Florbetapir F18 PET exams were acquired either at the VA Medical Center, San Francisco on a GE Discovery 690 PET scanner or at the China Basin Campus of the University of California, San Francisco on a GE Discovery STE VCT PET system. The participants were injected with 10 mCi (370 MBq) of florbetapir followed by 10 min PET acquisition 50 min later. The images were reconstructed and normalized to a florbetapir template on which several gray matter regions of interest known to be vulnerable to amyloid deposition in the temporal and parietal lobes, precuneus and anterior and posterior cingulate were labeled (Joshi et al. 2015). The mean count from each of these regions was extracted and regional Standard Uptake Value Ratios (SUVR) were calculated using whole cerebellum as the reference region. The global SUVR was calculated by averaging the SUVRs from the all cortical

Table 1 Subject Characteristics

	Amyloid negative $n = 30$	Amyloid positive $n = 19$
Age	70.2 (6.3)	71.3 (6.5)
SUVR	1.02 (0.06)	1.24 (0.11)*
ApoE4 pos/neg	7/23	8/11
CDR	0.0 (0.00)	0.03 (0.12)
MMSE	29.8 (0.5)	29.6 (0.8)
CVLT-II immediate recall discriminability	2.3 (0.4)	2.4 (0.7)
CVLT-II short free recall discriminability	2.6 (0.7)	2.5 (0.9)
CVLT-II delayed recall discriminability	2.6 (0.7)	2.5 (0.8)
DKEF Verbal Fluency	13.9 (3.33)	13.6 (3.3)
Digit Symbol	65.6 (17.1)	64.2 (13.7)

* $p < 0.5$

labels. Participants with a global SUVR equal or higher than 1.10 were considered to be amyloid positive.

MR acquisition

All images were acquired on a Siemens Skyra 3 T MR system equipped with a 20 channel receive coil. The following sequences were obtained as part of a larger research protocol. 1. T1-weighted gradient echo MRI (MPRAGE) of entire brain, TR/TE/TI = 2300/2.96/1000 ms, $1.0 \times 1.0 \times 1.0$ mm^3 resolution, acquisition time = 5.30 min for tissue segmentation. 2. PD/T2 weighted 2D turbo spin-echo sequence, TR = 3210, TE1/2 = 101/11 ms, $1.0 \times 1.0 \times 3.0$ mm^3 resolution, acquisition time: 3.43 min, for co-registration between T1 and EPI data. 3. 2D gradient echo EPI sequence TR/TE = 3000/30 ms, flip angle = 80, $2.5 \times 2.5 \times 3$ mm resolution, no gaps, acquisition time = 8.00 min for dynamic task-free analysis. Subjects were instructed to refrain from caffeinated beverages on the day of the exam, to close their eyes and to relax but stay awake and think of nothing in particular during the scan.

MR processing

SPM12 was used for the preprocessing of the structural and fMRI data (www.fil.ion.ucl.ac.uk/spm/). The T2 weighted image was co-registered to the T1 image. The T1 weighted images were segmented into tissue categories and the gray matter maps were warped onto a symmetrical gray matter atlas in MNI space using SPM12's DARTEL routine. The first 6 time frames were discarded to allow the MRI signal to achieve T1 equilibrium. The remaining 154 timeframes/subject underwent slice time correction, motion correction and realignment onto a mean EPI image in the T1 space, spatial normalization using the transformation matrices generated by DARTEL during the warping of the gray matter maps onto the gray matter template with re-sampling to a $1.5 \times 1.5 \times 1.5$ mm resolution. Framewise displacement (Power et al. 2012) was used to assess the motion during the exam. There was no significant difference between amyloid negative and amyloid positive CN (0.255 ± 0.119 vs. 0.2145 ± 0.07, $p = 0.19$). Conn 17a (www.nitrec.org/projects/conn/, Whitfield-Gabrieli and Nieto-Castagnon 2012) a SPM based toolbox for task and task-free fMRI analysis was used for further processing including linear detrending and band pass filtering (0.008–0.09 Hz) with simultaneous denoising. The latter included the aCompCorr routine to reduce the effects of physiological noise (eroded white and csf maps,5 components each) and motion regression (6 affine motion parameters and 6 first order temporal derivatives). In addition to that, ART as implemented in the conn preprocessing was used to identify timeframes with extreme fluctuations of the global signal (>z-score of 5) and/or motion exceeding a movement threshold of 0.9 mm (motion outliers). Conn disregards these timeframes during the denoising procedure but does not remove them and thus leaves the original time series intact. This resulted not only in a more efficient denoising of non-motion corrupted timeframes but also ensured that motion contaminated sections maintained the typical "motion signature" unaltered and thus were assigned to "motion clusters" during the next processing steps. No global signal removal was performed since this is known to falsely increase anticorrelations between time series (Murphy et al. 2009). The atlas of intrinsic connectivity of homotopic areas (AICHA, Joliot et al. 2015, cf. Fig. 1) consisting of 192 homotopic cortical, and subcortical region pairs was used to extract the mean time series and to estimate the functional connectivity.

Simulated data

Simulated data to characterize the graph analytical signatures of the two types of amyloid-associated hyperactivity discussed in the introduction was generated with SimTB (mialab.mrm.org/software/simtb, Erhardt et al. 2012). SimTB uses a data generation model consistent with spatio-

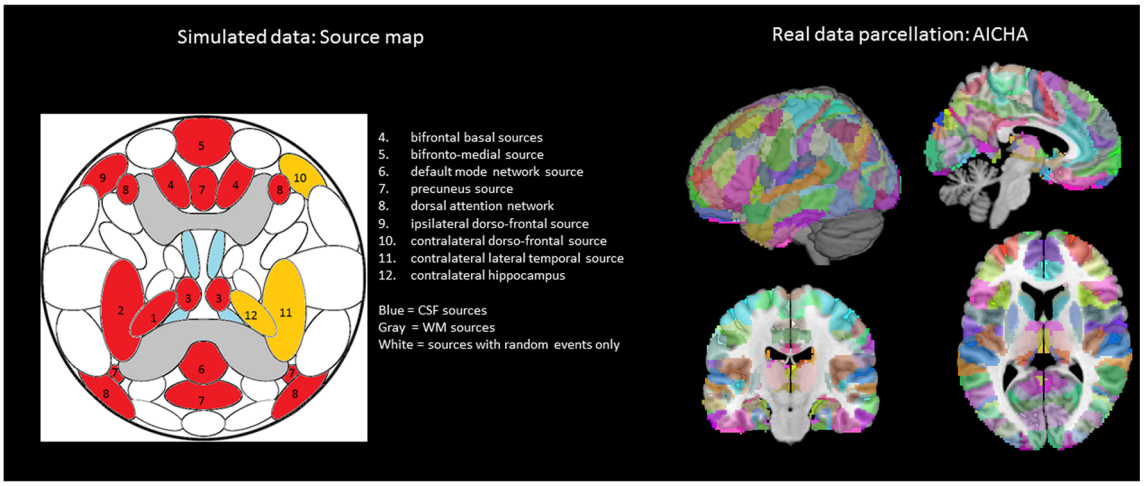

Fig. 1 Left Side: SimTB simulation: The sources of the default SimTB template that were used to model the two signals are highlighted in red (ipsilateral) and orange (contralateral). SimTB uses a data generation model that is consistent with spatiotemporal separability, i.e. the activations are expressed as a linear combination of amplitude scaled and baseline shifted time courses and spatial map sources. The connection between different spatial maps is determined by their closeness to each other, i.e., long-distance correlations that are known to exist in real data are not modeled. The localization of the spatial maps and their spatial extent are slightly varied to introduce some variations between subjects and Gaussian noise is added so that each subject spatial map is unique. The time courses were generated by adding amplitude scaled task/event related and randomly occurring unique events and convolving it with a canonical hemodynamic response function, scaling it to have a peak-to-peak range of one and adding Gaussian noise. The resulting time courses and the spatial maps scaled by component amplitudes are combined and then scaled to a tissue weighted baseline to generate the no-noise data. The final noise data is generated by adding motion and Rician noise. Please see Erhardt et al. 2012 for details. Right side: AICHA (atlas of intrinsic connectivity of homotopic areas) parcellation used to extract BOLD signals in real data

temporal separability, i.e., it simulates data as a product of spatial maps and time courses. The SimTB standard template with 30 partially overlapping spatial maps was used to model task-free activity and task-free activity with short hyperactivity episodes (Fig. 1, please refer to legend for a summary how the signal is modeled in SimTB). Except for the modifications relating to the hyperactivity episodes, the parameters of the experiment described in Erhardt et al. 2012 were used in this study. Task-free data without episodes of the two amyloid associated hyperactivity types (baseline) was simulated for 33 subjects, each with 30 sources or ROIs of which two were allocated to CSF and two to white matter in a dataset of 148 × 148 voxels and 230 timepoints collected with a TR of 3 s. To mimic the effect of mild motion, the sources of each subject were allowed a translation up to max 0.02 of the entire image length and a rotation of up to max 5 degree for each sample. Unique events that occurred with a probability of 0.35 at each TR for all sources were used to simulate BOLD signal fluctuations in the absence of amyloid associated abnormalities. Their amplitude was kept constant at 0.8 for tissue sources and at 0.05 for the CSF sources. Amplitude and probability of the unique events were determined by testing a range of parameters (0.2–1 for amplitude and 0.2–0.4 for probability) and choosing those that produced baseline data that showed similar short spontaneous phases of mildly increased pos strength/decreased neg strength after processing as those seen in the data from amyloid neg CN (cf. Fig. 2). Two types of amyloid associated hyperactivity episodes were evaluated: 1. Epileptiform or spike-like (spike). The effects of epileptiform discharges on the BOLD signal have been intensively studied in epilepsy patients who underwent simultaneous EEG recordings to identify epochs with epileptiform activity. The BOLD changes associated with the epileptic discharge appear with a 4–6 s delay and last about 10 s. Initially, they are typically positive and focal but can become widespread and - if they involve the default network – negative in later phases. In short, the isolated epileptogenic spike behaves in many ways like a very short, albeit non-physiological activation task with synchronized BOLD signal fluctuations over several brain regions that will disrupt the typical task-free connectivity patterns in a complex way (Wennberg et al. 2011, Faizo et al. 2014, Lopes et al. 2014, Liu et al. 2014, Kay et al. 2014, Bai et al. 2011, Mishra et al. 2013). The spike signal was therefore modeled as a short (<1TR) activation (linear convolution with canonical hemodynamic response function) with decaying amplitude that appeared first in the left hippocampus source (amplitude 2.0) before spreading with a delay of 0.2 s for each step to the ipsilateral temporal lobe (amplitude 2.0) and thalamus (amplitude 1.8) sources, to the bi-frontal basal

Fig. 2 Examples positive (pos) and negative (neg) strength maps for ▶ simulated data and real data. The x axis represents the regions of interest (1–30 for simulated data, 1–384 for real data, The y-axis the represents windows (1–214 for simulated data and 138 for real data). The window during which the spike and hyper signal were modeled are indicated with "spike" and "synchron"

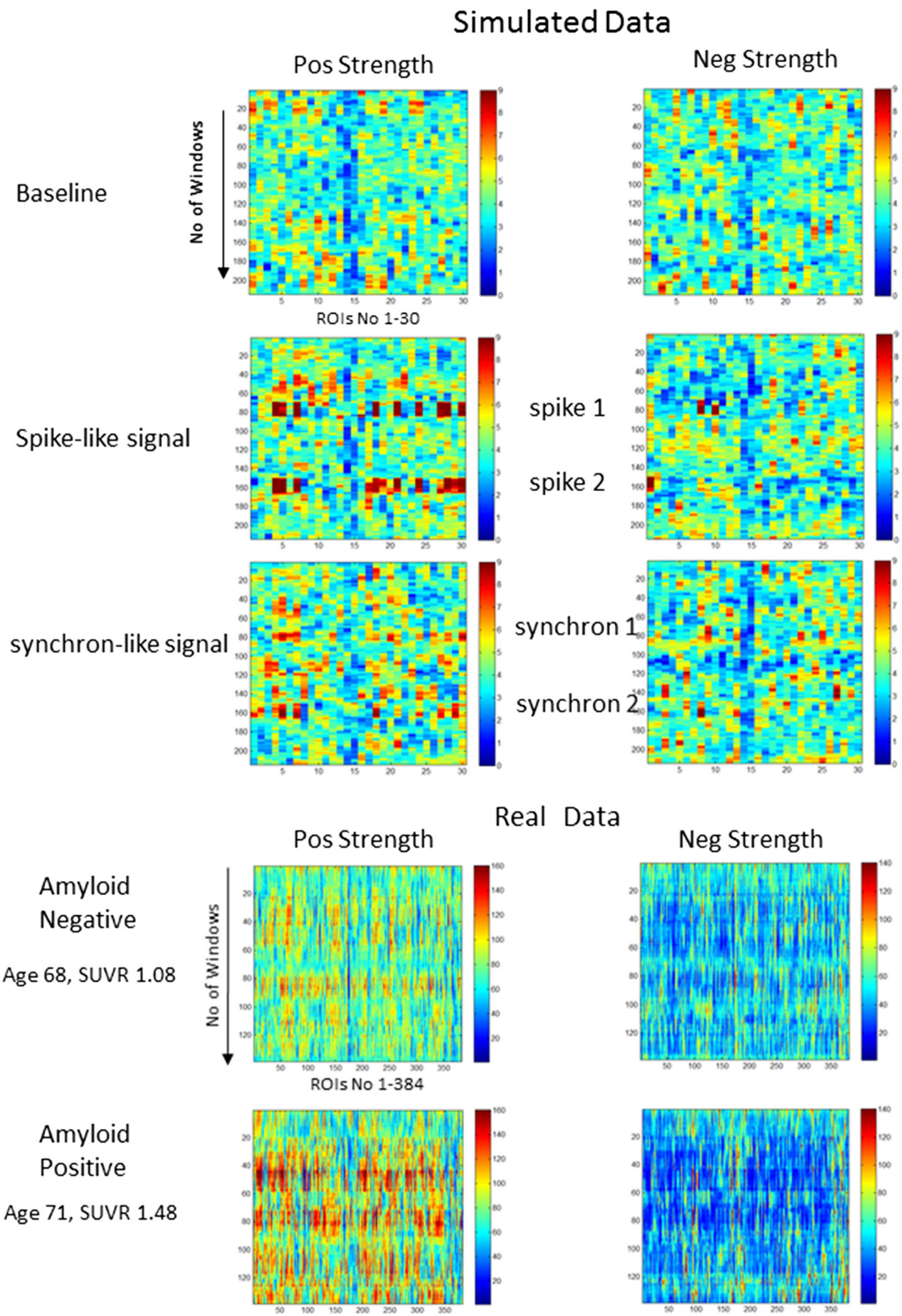
Simulated Data
Pos Strength
Neg Strength
Baseline
No of Windows
ROIs No 1-30
Spike-like signal
spike 1
spike 2
synchron-like signal
synchron 1
synchron 2
Real Data
Pos Strength
Neg Strength
Amyloid Negative
Age 68, SUVR 1.08
No of Windows
ROIs No 1-384
Amyloid Positive
Age 71, SUVR 1.48

sources (amplitude 1.8) and fronto-medial source (amplitude 0.05), the dorsal attention network sources (amplitude 1.5) and the frontal lateral sources (amplitude ipsilateral 1.8, contralateral 1.5), the precuneus (amplitude 1.0) and DMN sources (amplitude −1.0) and finally to the contralateral hippocampus (amplitude 1.0) and temporal lobe source (amplitude 1.0). The activity of the remaining sources was modeled with randomly occurring unique events (probability: 0.35, amplitude 0.8). The signal spread used in this simulation mimicked one of the possible propagation patterns seen in epileptic discharges in temporal lobe epilepsy (TLE) to account for the finding that epileptiform discharges in AD patients are predominantly observed in the temporal regions (Vossel et al. 2013). It has to be emphasized though that because of the use of global strength fluctuations instead of source-wise or ROI-wise fluctuations for the next processing steps, the order of the spread or the sources used to model the signal does not really matter. 2. Diffuse slowing or weak hypersynchrony-like (synchron). In contrast to the BOLD signal of the epileptogenic signal, there exists only one task-free fMRI study in an animal model (Shah et al. 2016) that describes this abnormality as hypersynchronous event encompassing hippocampus medial temporal structures, thalamus, DMN and cingulate. The synchron activity was modeled as a short activation with the same amplitude as the random signal (amplitude 0.8) that occurred simultaneously in the same sources involved in generating the spike model. 66 data sets were simulated with these parameters (33 with 2 spike-like 80 TR apart, i.e., between windows 70–85 and 150–165, 33 with 2 synchron BOLD signals 80 TR apart, i.e., between windows 70–85 and 150–165). They were compared to the 33 simulated data sets with baseline activity.

Variants of the two signals of interest were also explored to investigate effects of spatial extent (number of sources showing the signal), duration of the signal or occurrence of both signal types in the same data set on the graph analytical signature. More restricted patterns, e.g. spike or synchron phases restricted to one or two regions, did not produces a signature that could reliably be observed with the global approach used in this study and their appearance in the strength maps was not consistent with the appearance of a widespread disturbance observed in the strength map of the real data. This was also the reason why the spike signal was modeled as a widespread bilateral event that is more commonly associated with epileptiform discharges in primary generalized epilepsy although this type of widespread discharge can also be observed in focal epilepsy (An et al. 2015). More complex signals, e.g. longer spike or synchron phases (3 TR instead of 1 TR), spikes with shorter propagation times, synchron with propagation) typically resulted in more complex cluster patterns that were not observed in the real data and thus also not further explored.

Dynamic functional connectivity analysis and graph analysis

A sliding windows approach was used to detect episodic hyperactivity in real data and the effects of the two simulated hyperactivity types in simulated data. Based on observations that robust estimations of the functional connectivity without loss of potentially interesting fluctuations are possible with window sizes around 30–60 s (Hutchison et al. 2013), a 45 s window (15 timeframes) was chosen that was advanced with increments of one TR along the artifact corrected time series resulting in 138 windows/subject or 6762 windows for all 49 subjects and in 214 windows/subject or 7062 windows for each of the three simulated data sets.

Graph analysis (Sporns et al. 2000) was used to characterize the interactions between the different ROIs in each window. Graph analysis describes a network as a system of nodes and edges that connect nodes with similar properties. In terms of in vivo imaging, nodes correspond to ROIs for which the property of interest, e.g., mean time course of the BOLD signal in a ROI, is known and the edges represent the strength of the correlation between any two ROIs based on the similarity of this property. The result is a correlation matrix that describes this relationship for every possible combination of ROIs. Several graph analytical measures can be calculated to further characterize the network. In this project measures for modularity and centrality that allowed to investigate the dynamic behavior of fully connected matrices with positive and negative correlations (https://sites.google.com/site/bctnet/measures/, Rubinov and Sporns 2010, 2011) were chosen since they are better suited to detect complex changes of connectivity patterns than more traditional measures based on sparse positive connections alone. Positive and negative strength provide a measure of the intensity of the correlations between a specific node with the other nodes in the network and indicate if these connections are based more on positive than negative correlations. The existence of negative connections or anti-correlations in task-free data had initially been questioned after it had been shown that regressing out the global signal intensity introduced spurious negative correlations (Murphy et al. 2009). However, since then several studies that acquired EEG and fMRI data simultaneously provided support that negative correlations represent indeed a neurophysiological phenomenon (Carbonell et al. 2014; Chai et al. 2012; Keller et al. 2013; Chang et al. 2013). Hyperactivity was expected to be associated with increased positive strength and simultaneously decreased negative strength reflecting the more widespread than usual synchronized (synchron) or near-synchronized (spike) activity. Modules are groups of nodes or brain regions that share high positive correlations between each other but mostly weak or no connections with brain regions not belonging to this group. The modularity algorithm (modularity_finetune_und_sign was applied 100 times to each window and the partition with

the highest modularity Q* (average difference between within module connection weights present and by chance expected within module connection weights (cf. Rubinov and Sporns 2011 for details of the algorithm and definition of Q*) and highest frequency was selected. Diversity finally provides information about the strength of the connections between nodes within the same module compared to the strength of connections to nodes from other modules. A high value means that the nodes or brain region have also strong correlations with other brain regions that do not belong to their group or module, a low value means that only very few such correlations exist. Diversity allows to further characterize high strength nodes by distinguishing between those that connect modules (high strength, high diversity) and those that separate modules (high strength, low diversity). It was expected that the graph analytical signature of spike would be dominated by separated high strength nodes and that of synchron by connected high strength nodes. Please see Fig. 2 for representative maps of the fluctuations of positive and negative strength in simulated and real data.

Characterization of different activity states in real and simulated data with hierarchical cluster analysis

Real data: Nodal positive and negative strength in each window were converted into nodal z-scores using mean and standard deviation of the nodal strength of the amyloid neg CI as reference with the following formula: strength z-score of node x in window n = strength of node x in window n – mean of strength of node x from all windows in reference data set/ standard deviation of strength of node x from all windows in reference data set. The calculation of z-scores served two purposes. 1. To ensure that fluctuations of neg and pos strength were weighted equally in the cluster analysis. 2. To correct for the differences in strength between real data and simulated data due to the different number of nodes when comparing the graph analytical signatures of the real data cluster with those of the simulated data. The thus calculated nodal z-scores/window were averaged over all nodes to obtain global positive and negative strength z-scores for each window in each subject. Hierarchical cluster analysis (Ward's minimum variance methods with the cubic clustering criterion to identify optimal cluster number) was used to identify different global negative and positive strength profiles representing different states of activity. Entering the global positive and negative strength z-scores/window of amyloid pos and neg subjects together in the cluster analysis identified 11 different clusters or activity states in the real data. Please see Fig. 3.

The output generated by ART was used to identify windows with motion outliers in the real data and to calculate the % of motion outliers for each cluster. Clusters 9–11 consisted of more than 50% of motion outliers (range 75–100%) and therefore were considered to represent "motion clusters" and were not further evaluated. 38.6% of the windows assigned to cluster 1 had been identified as motion outliers and therefore cluster 1 was considered as "motion contaminated. All other clusters had 20% or less motion outliers and were together with cluster 1 fully evaluated after excluding all motion outlier windows. Eliminating windows with excessive motion results in a more rigorous elimination of motion artifacts than just eliminating the motion affected timeframe alone because it also eliminates timeframes with subthreshold motion that usually accompany timeframes with suprathreshold motion.

After assigning each window to a cluster based on its global strength profile the next step was to investigate if certain clusters tended to occur together. This was done by calculating the "cluster neighborhood" or the frequency by which a window that had been assigned to cluster A were next to a window assigned to one of the other clusters in a data set. The frequencies with which the other clusters appeared were compared with Fisher's exact test ($p < 0.05$ with Bonferroni correction for multiple comparisons) to identify those cluster(s) that were significantly more often found in the neighborhood of cluster A than others clusters.

Simulated data: The simulated data was similarly processed as the real data. Nodal positive and negative strength in each window were first converted into nodal z-scores using the mean and standard deviation of the nodal strength of the baseline data sets as reference and then global positive and negative strength z-scores for each window calculated. To mimic the mixture of data from subjects with low (amyloid neg) and high (amyloid pos) probability to experience hyperactivity found in real data, the global positive and negative strength z-scores/window of the "spike" data set and of the baseline data set were entered together in the hierarchical cluster analysis. This identified 8 different clusters or activity state. The synchron data set was processed in the same way and 13 different clusters/activity states identified. Cluster neighborhood was calculated for each of the two simulated data sets in the same way as had been done for real data.

Matching graph analytical signatures in real data with simulated data signatures

The graph analytical signature of the spike-like and the synchron -like signals is characterized by a single or more likely a group of clusters that occur almost exclusively during spike and synchron phases. Each of these clusters is defined by a specific profile of its means of pos and neg strength and pos and neg diversity. In order to identify which set of signal clusters represented a better match to the clusters found in real data, these means were converted into a graphical representation or signature map (please see Fig. 4a). A weighted dice coefficient was calculated between each and every signature

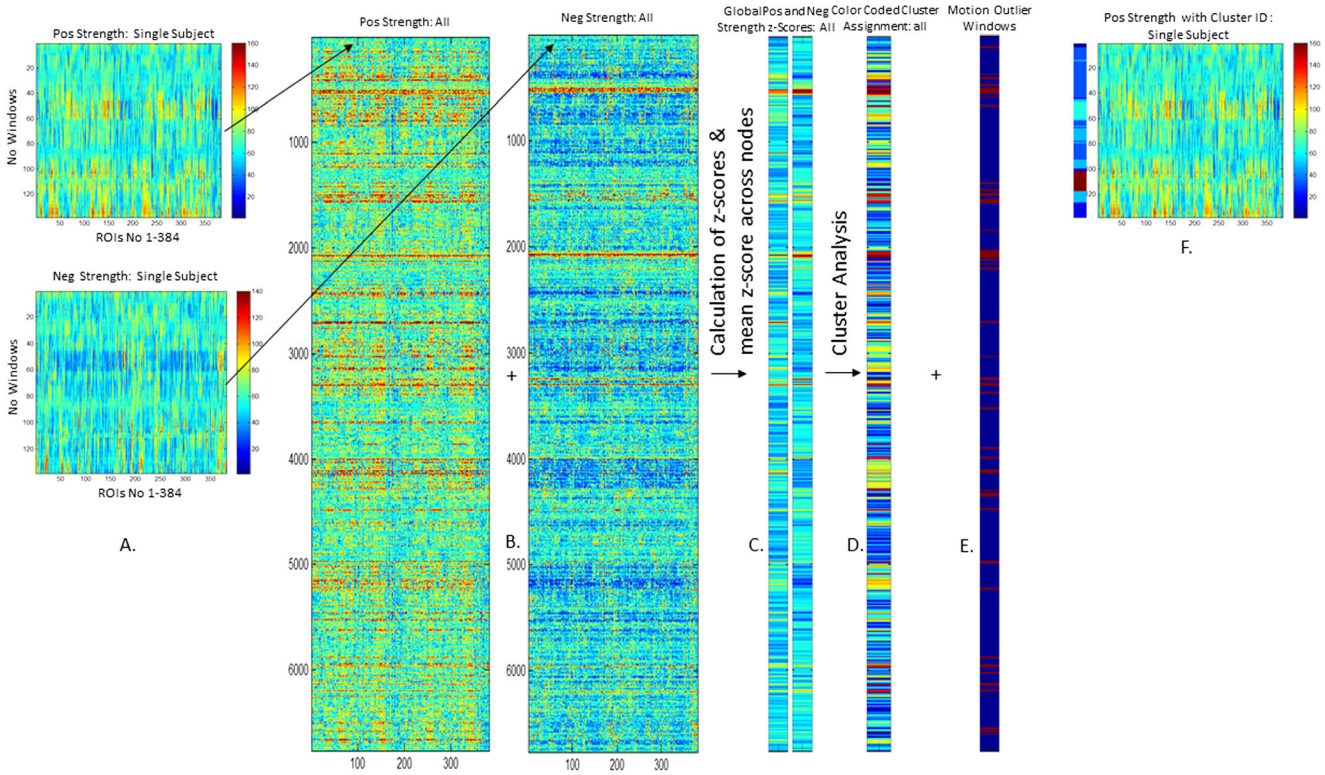

Fig. 3 Overview of processing steps. An example of a strength maps of an amyloid neg subject is depicted on the right side (**a**). For the analysis the strength maps of all 49 subjects were combined (**b**), converted into nodal z-scores using the mean and std. from the amyloid neg CN group as a reference from which the global pos and neg strength mean z-scores/window were calculated by averaging the nodal pos strength and neg strength z-scores of each window (**c**). The global pos and neg strength mean z-score/window were used as the input for a hierarchical cluster analysis to identify clusters of windows with a similar global pos and neg strength profiles representing different activity states. The cluster analysis identified 11 different clusters, each is coded by a different color (**d**) The output from ART was used to identify windows with excessive motion or global signal fluctuations (**e**) and to eliminate them from all further analyses. Dark blue indicates windows without excessive motion, red indicates windows with excessive motion that will be excluded from the analysis. The right-most panel shows sample subject (**f**). The color bar to the left of the pos strength map represent the color coded clusters or activity states that have been detected in this subject. The red zone indicates windows with excessive motion that were omitted from the analysis

map of the simulated data and each and every signature map of the real data. The weighting was applied to both strength means that were counted double to emphasize that pos and neg strength had not only been used to define the clusters but also because they spanned a larger range than the diversity means and thus contributed more to distinguish the clusters. The real data cluster that had the highest dice coefficient with the hyperactivity associated clusters in the simulated data was identified (Fig. 4 b). The hyperactivity type with the higher dice in this comparison was deemed to capture the nature of disturbance causing hyperactivity episodes in real data better than the one with the lower dice.

Stationary analysis

Global (average over all nodes) and nodal positive and negative strength were calculated for each subject from the each subject's whole time series after removing motion outlier timeframes.

Statistics

Dynamic analysis Mann Whitney and one tailed Spearman correlation tests were used to test for differences of the occurrences of different clusters between amyloid pos and amyloid neg CN and to investigate the relationship between cluster counts and module frequency and SUVR, age and cognitive function. Given the a priori hypotheses stated in the introduction, no correction for multiple comparisons was performed for findings in accordance with those hypotheses (positive correlation of number of windows with hyperactivity signature/subject with SUVR and negative with measures of memory performance). JMP 12.1.0 was used for statistical analyses,.

Stationary analysis Mann Whitney tests to assess group effects and two-tailed Spearman correlation analyses corrected for multiple comparisons (FDR $p < 0.05$) were used to assess global and each nodes strength with SUVR and memory performance.

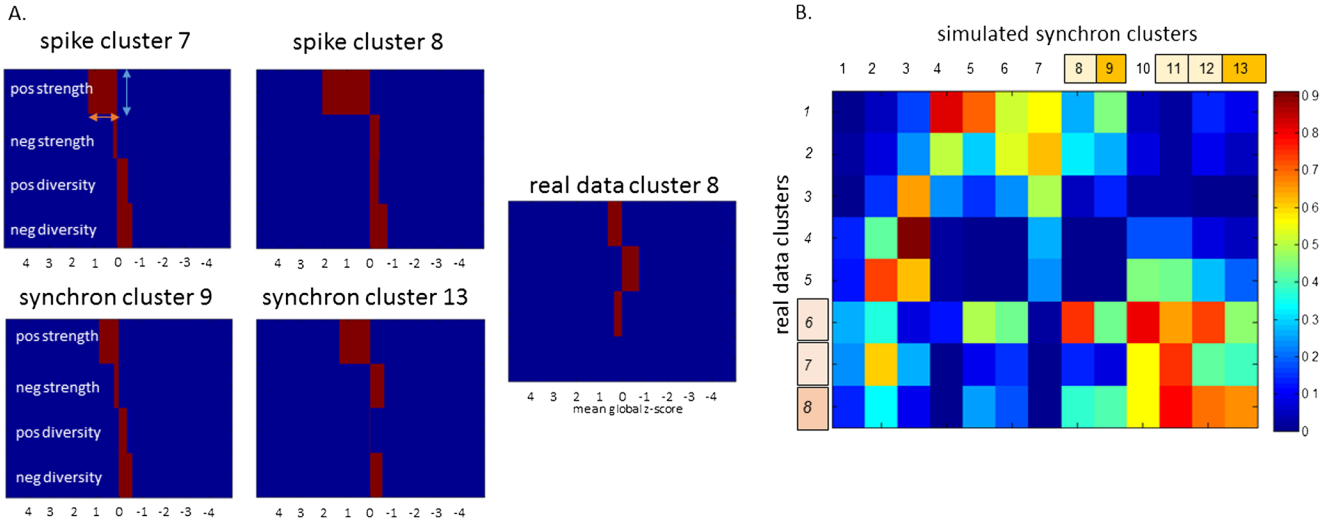

Fig. 4 a. Examples of signature maps. Upper row spike signature maps of simulated data, lower row, hyper signature maps of the simulated data. Signature map of real data cluster 8. The four red blocks represent the cluster means of positive strengths, negative strength, positive diversity and negative diversity. The height (blue arrow spike cluster 7) of each block is 1, the length (red arrow) corresponds to the mean global z-score of the measure (cf Table 2). 4 b. Dice coefficient map of the signature maps of the hyper-like simulated data and the real data clusters. The tan colored cluster numbers correspond to the two clusters predominantly found during hyper windows, the lighter colored clusters represent the background clusters associated with them. Real data cluster 8 associated with SUVR and cognition is indicated with light red. Its associated neighboring clusters or background clusters are highlighted with pale red

Results

Dynamic connectivity analysis

Simulated data

Characterization of the "spike" and "synchron" graph analytical signatures The strength profiles of the 8 clusters identified in the base/spike population and of the 13 clusters identified in the base/synchron population are shown in Tables 2 and 3. The activity clusters observed in the epochs during which the spike and synchron signals had been introduced (windows 70–85 and windows 150–165) were compared with those seen in the baseline data sets in these windows. It was assumed that clusters that were only or predominantly observed in windows 70–85 and 150–165 of the spike and synchron data sets but not outside of these windows or in the baseline data sets represented activity that was associated with the two signals of interest.

Base/spike data set: Please see also Table 2. Windows 70–85 and 150–165 contained 91.8% of all windows assigned to cluster 7 and 97.1% of all windows assigned to cluster 8. In accordance, the frequency of windows assigned to cluster 7 and 8 outside spike epochs and in the baseline data was low.

Table 2 Strength and diversity profiles of spike signal clusters

Cluster	Window count	meanSposZ	meanSnegZ	meanDposZ	meanDnegZ	Neighboring clusters	Assignment
1	3537	0.073	−0.166	0.084	0.032	**4, 6,** 2, 3	background
2	863	0.605	0.010	−0.116	−0.264	**1**	spike background
3	649	0.536	−0.533	0.187	−0.089	**1,** 2	spike background
4	2587	0.114	0.170	−0.081	−0.080	**1,** 5, 6	background
5	1636	0.194	0.485	−0.307	−0.261	**4,** 6	background
6	3945	−0.254	0.073	0.044	0.140	**1, 4,** 5	background
7	596	1.280	0.176	−0.473	−0.663	**2, 8,** 3	balanced simple spike/complex spike
8	311	2.106	−0.419	−0.379	−0.751	**7, 3**	unbalanced complex spike

neighboring clusters, appear significantly more often with this cluster than other clusters, bold clusters appear significantly more often with this cluster than non-bold clusters listed in column

meanSposZ, mean of pos strength z-score (please see methods for details) in cluster

meanSnegZ, mean of neg strength z-score in cluster

meanDposZ, mean of pos diversity z-score (please see methods for details) in cluster

meanDnegZ, mean of neg diversity z-score in cluster

Table 3 Strength and diversity profiles of hypersynchronous signal clusters

Cluster	Window count	meanSposZ	meanSnegZ	meanDposZ	meanDnegZ	Neighboring clusters	Assignment
1	1592	0.063	−0.040	0.013	−0.012	**2, 6,3,7,** 8,10	background
2	1586	−0.031	−0.253	0.125	0.078	**1, 3,** 10, 11	background
3	3037	−0.307	−0.047	0.085	0.165	**7,** 2, 1	background
4	741	−0.012	0.461	−0.257	−0.142	**7**	background
5	296	0.362	0.552	−0.428	−0.425	**6,** 4	background
6	1185	0.180	0.215	−0.176	−0.184	**1, 7, 8,** 5	background
7	2497	−0.124	0.224	−0.073	0.008	**3, 4, 1, 6**	background
8	810	0.410	0.035	−0.093	−0.246	**1, 6,** 10, 12	balanced hyper background
9	164	0.868	0.229	−0.358	−0.582	**8**	balanced hyper
10	618	0.307	−0.267	0.083	−0.080	**2, 11, 1, 8,** 12	background
11	732	0.336	−0.565	0.209	−0.034	**10, 2, 12**	unbalanced hyper background
12	640	0.714	−0.310	0.002	−0.287	**11,** 8, 10, 13	unbalanced hyper background
13	226	1.356	−0.612	0.016	−0.515	**12, 11**	unbalanced hyper

neighboring clusters, appear significantly more often with this cluster than other clusters, bold clusters appear significantly more often with this cluster than non-bold clusters listed in column

meanSposZ, mean of pos strength z-score (please see methods for details) in cluster

meanSnegZ, mean of neg strength z-score in cluster

meanDposZ, mean of pos diversity z-score (please see methods for details) in cluster

meanDnegZ, mean of neg diversity z-score in cluster

The frequencies of windows assigned to clusters 1–6 were low in windows 70–85 and 150–165, i.e., during spike epochs. Based on these observations, it was concluded that cluster 7 and 8 activity represented the graph analytical signature of the spike signal. The neighborhood frequency analysis indicated that cluster 7 windows occurred together with cluster 8 and cluster 2 windows in spike epochs. Cluster 8 windows were mostly associated with cluster 7 but also with cluster 3 windows. The presence of windows assigned to clusters 7 and/or 8 identified 65/66 spike epochs. 47.7% of the epochs were defined by a combination of cluster 7 and 8. 47.7% were identified by windows assigned to cluster 7 alone and less than 1% by those assigned to cluster 8 alone. Please see Table 2a for the strength and diversity profiles of cluster 7 and 8. Cluster 2 had a similar but less prominent profile as cluster 7 and cluster 3 had a similar but less prominent profile as cluster 8. Based on these observations clusters 2 and 3 were considered to represent baseline activity that transitioned into the pattern of cluster 7 (simple spike pattern) or a mixture of cluster 7 and 8 (complex spike pattern) with the application of the spike signal.

Base/synchron data set: Please see also Table 3. Windows 70–85 and 150–165 contained 74% of all windows assigned to cluster 9 and 81% of all windows assigned to cluster 13. The frequency of the other clusters during synchron periods ranged between 0.5% (cluster 3) and 44% (cluster 12). The graph analytical signatures of cluster 9 and 13 were therefore considered to represent the synchron signal. The neighborhood frequency analysis indicated an association of cluster 9 with cluster 8 windows and an association of cluster 13 windows with cluster 12 windows. The presence of windows assigned to clusters 9 and 13 identified 38/66 synchron epochs. 18 episodes were identified by cluster 13 windows alone and 10 by cluster 9 windows alone. 10 synchron episodes were identified by a combination of cluster 9 and cluster 13. Please see Table 3 for the strength and diversity profiles of clusters 9 and 13. Cluster 8 had a similar strength/diversity profile as synchron cluster 9 and was therefore considered to represent a background activity that transitioned into cluster 9 activity with the application of the synchron signal. The same applied to clusters 11 and 12 who appeared together with synchron cluster 13.

Real data

The strength profile of the 11 clusters identified in amyloid pos and neg CN including the information about cluster neighbors is shown in Table 4. Compared to the strength profiles of the simulated data, the percentage of clusters with decreased positive strength was higher in real data than in the spike data sets (45.5% vs 12.5%) and the synchron data sets (45.5% vs 30.8%) indicating a more balanced strength profile in real data than in simulated data. Cluster 8 was the only real data cluster whose graph analytical signature corresponded to the hypothesized "hyperactivity" pattern.

Comparison to "spike" simulation: The strength/diversity profile of spike cluster 7 was closest to that of the motion contaminated real data cluster 1 (signature map dice

Table 4 Strength and diversity profiles of real data clusters after removal of motion outlier windows

Cluster	Window count	% motion outlier windows before removal	Mean fwd after removal of motion outlier	meanSposZ	meanSnegZ	meanDposZ	meanDnegZ	Neighboring Clusters	No amyloid neg / No amyloid pos	Assignment
1	194	39	0.26	−0.116	0.448	−0.461	−0.298	**2,** 3	19/11	background
2	973	11	0.24	−0.096	0.085	−0.179	−0.145	**4**	28/19	background
3	941	1	0.19	−0.490	0.155	0.041	0.234	**4,** 2	23/18	background
4	1251	0	0.22	−0.330	−0.068	0.141	0.229	**5,** 2, 3	30/18	background
5	986	0	0.23	−0.183	−0.259	0.232	0.227	**4,** 7	28/19	background
6	452	21	0.24	0.362	−0.197	−0.024	−0.261	**7, 2**	23/12	amyloid background
7	785	0	0.24	0.101	−0.476	0.289	0.150	**5,** 8, 6	22/16	amyloid background
8	302	8	0.25	0.618	−0.727	0.351	−0.002	**7,** 6	14/7	amyloid
9	13	75	0.29	1.325	−0.375	−0.048	−0.755	na	7/0	motion
10	31	90	0.31	0.506	0.389	−0.218	−0.286	na	10/8	motion
11	0	100	na	na	na	na	na	na	0/0	motion

neighboring clusters, appear significantly more often with this cluster than other clusters, bold clusters appear significantly more often with this cluster than non-bold clusters listed in this column.

na, not available, mean fwd, mean framewise displacement/window in cluster

meanSposZ, mean of pos strength z-score (please see methods for details) in cluster

meanSnegZ, mean of neg strength z-score in cluster

meanDposZ, mean of pos diversity z-score (please see methods for details) in cluster

meanDnegZ, mean of neg diversity z-score in cluster

amyloid, cluster counts associated with SUVR

co-efficient 0.38) and that of spike cluster 8 was closest to real data cluster 8 (signature map dice co-efficient 0.45). Both dice coefficients were low indicating that the spike signal was not a good match for the real data.

Comparison to "synchron" simulation: The strength/diversity profile of synchron cluster 9 was closest to the profile of the motion contaminated real data cluster 1 with a signature map dice co-efficient of 0.44 which was considered to be too low to be a good match for real data. The strength/diversity profile of synchron cluster 13 matched the signature of real data cluster 8 with a signature map dice co-efficient 0.66 reasonably well though. The strengths/diversity profiles of real data cluster 8 and that of one its neighboring clusters (real data cluster 6) also matched the profile of cluster 12 that had been identified as the background activity of synchron cluster 13 reasonably well (signature map dice co-efficient with real data cluster 8 was 0.69 and 0.74 with real data cluster 6). The strength/diversity profile of real data cluster 7 that was more commonly associated with real data cluster 8.than cluster 6 matched the profile of simulated cluster 11 (dice coefficient 0.75) well but less so that of cluster 12 (dice coefficient 0.42). Taken together, the strength and diversity profile of synchron cluster 13 and its background activity clusters 12 and 11 were reasonably well matched with the strength and diversity profile of real data cluster 8 and its neighboring clusters 7 and 6.

To test the relationship between amyloid load and occurrence of real data cluster 8, the number of windows which had been assigned to this cluster were counted in each subject. The Spearman rank correlation coefficient between the total number of cluster 8 windows/subject in those subjects in whom this cluster was present ($n = 21$) and their SUVR was $r = 0.42$ $p = 0.03$. The median count of cluster 8 windows was 11 (range: 1–31) in amyloid neg CN and 17 (range 4–49) in amyloid pos CN. Significant correlations between window counts/subject and SUVR were only found for cluster 8.

The memory performance of subjects with cluster 8 windows did not significantly differ from those without cluster 8 windows (cluster 8 no/yes: immediate recall: 2.3 ± 0.4 vs 2.3 ± 0.6; short free recall: 2.5 ± 0.7 vs 2.6 ± 0.8; delayed recall: 2.5 ± 0.7 vs 2.6 ± 0.8). However within the group of subjects who had cluster 8, the total number of cluster 8 window/subject was negatively correlated with immediate free recall ($r = -0.38$, $p = 0.049$), short free recall ($r = -0.43$, $p = 0.03$ and delayed recall discriminability ($r = -0.40$, $p = 0.042$). Neither immediate free recall ($r = -0.06$, $p = 0.40$), short free recall ($r = 0.36$, $p = 0.06$) nor delayed recall discriminability ($r = -0.31$, $p = 0.09$) were correlated with SUVR.

Effects of motion

Dynamic task-free fMRI data processing approaches are particularly sensitive to head motion that can introduce artificial signal fluctuations mimicking temporary changes in connectivity patterns (Hutchison et al. 2013). To account for that a modification of data scrubbing (Powers et al. 2014, 2015) was used in this study to eliminate windows containing timeframes with excessive motion. To investigate the influence of the remaining motion on the association of cluster 8 window counts with SUVR etc., the median framewise displacement/window was calculated for each subject with cluster 8 windows using the same sliding window parameters that had been used to subdivide the BOLD data timecourses. It was assumed that if motion indeed induced a particular strength/diversity pattern and thus generated motion driven cluster profile(s), subjects with more motion artifacts should have higher counts of these clusters, i.e., the counts of motion driven clusters should be positively correlated with the motion in these subjects. The cluster 8 counts/subject did not correlate with the median framewise displacement/window in subjects with cluster 8 windows ($r = 0.03$, $p = 0.45$). The same associations between real cluster 8 window counts and SUVR etc. were also found, when the analysis was restricted to subjects without motion outlier windows during cluster 8 windows (no of subjects = 17, Spearman rank correlation cluster 8 window counts with SUVR: $r = 0.52$ $p = 0.02$, immediate free recall: $r = -0.43$, $p = 0.049$, short free recall: $r = -0.45$, $p = 0.039$, delayed discriminability $r = -0.48$, $p = 0.03$) median framewise displacement: $r = 0.16$, $p = 0.27$). Finally, SUVR was significantly negatively correlated with subject motion ($r = -0.293$, $p = 0.02$) which indicates that that amyloid positivity was associated with less motion rather than more motion.

Based on these results and on those in the previous section, it is concluded that it is very unlikely that the correlations between SUVR and cluster 8 window counts were caused by motion.

Stationary analysis

There were no significant associations between global stationary strength and SUVR or memory performance. At the level of individual nodes, the neg strength of a node situated in the left precuneus was negatively correlated with SUVR ($r = -0.46$, $p = 0.001$) but not with any of the cognitive measures. Neg strength of this node was decreased in amyloid pos CN compared to amyloid neg CN (15.4 ± 3.6 vs 19.8 ± 6.2, $p = 0.01$) its pos strength was not different between the two groups.

Discussion

This study used dynamic functional connectivity analysis and graph analysis to investigate if amyloid causes intermittent functional connectivity disturbances consistent with intermittent hyperactivity in brains of cognitively intact elderly subjects with and without increased amyloid load. Based on the

electrophysiological characteristics of intermittent amyloid-induced hyperactivity observed in AD animal models and EEG abnormalities in patients with MCI and AD, two types of intermittent hyperactivity, spike and synchron, were characterized in simulated data and compared to the findings in real task-free fMRI data. There were two major findings: 1. The simulation showed that the two types of hyperactivity had similar but nonetheless sufficiently different graph analytical profiles to be distinguished from each other. 2. Analyzing real data with the same approach identified phases of activity whose graph analytical signature was consistent with a hyperactivity episode and resembled the simulated synchron signature. The duration of these phases was positively correlated with amyloid load and negatively with memory performance. Taken together, dynamic connectivity analysis combined with graph analysis found intermittent amyloid load associated disturbances of functional connectivity consistent with phases of hypersynchronous hyperactivity. The only evidence for a disturbed functional connectivity in the stationary analysis was a decreased neg strength in the left precuneus in amyloid pos CN that was also negatively correlated with SUVR. In the following paragraphs potential interpretations of these dynamic disturbances and their potential impact on cognitive processes will be discussed.

Simulated data

Data sets containing two different of types of short hyperactivity episodes were generated and their graph analytical signature characterized by comparing them to the graph analytical patterns caused by random events. The two hyperactivity types generated two slightly different responses. Both responses were characterized by an increased positive strength as expected but one was accompanied by decreased negative strength (unbalanced) also expected and the other by a normal or increased negative strength (balanced) which had not been expected. In the case of the spike-like hyperactivity the balanced and unbalanced types were observed together in roughly half of the spike episodes. The remaining spike episodes showed only the balanced type. In the case of the synchron -like signal, the balanced and unbalanced types were not observed together. Since the hyperactivity model was kept constant in all data sets it is possible to exclude what would have been one of the obvious explanations for such an observation in real data, i.e., varying severity or varying spreading patterns of the hyperactivity. This leaves the alternative explanation that the appearance of the hyperactivity response is influenced by the background activity at the time of its occurrence. This explanation is supported by the neighborhood analysis that showed that both hyperactivity responses were embedded in background activity with a graph analytical signature similar to their own. The most obvious difference between the two signal types was the frequency with which they were able to induce a noticeable change of the random background activity. While the spike-like signal produced a response with a characteristic graph analytical profile signature in 98% of the of the spike epochs, the synchron -like signal did so only in 58% of the synchron epochs. The lower detectability of the synchron signal could not simply be explained by the presence of the "wrong type" of background activity during application of the signal since one of the two background activities associated with the synchron signal was present in 53% of the epochs without a detectable synchron signature. Simulations with both signals using different parameters, e.g., length, repeats, motion etc., had shown that the number of sources showing the signal, and signal amplitude were the two main factors that determined if the signal was detected by the global approach used in this study. Since the number of sources was the same but the amplitudes of the spike-like signal were clearly higher than those of the random background activity or those of the synchron -like signal, the lower amplitude of the synchron signal is the most likely explanation for this difference. Taken together, both hyperactivity types exaggerated the background activity at the time of their occurrence and thereby created two different hyperactivity states (balanced vs. unbalanced).

Real data

The same analysis approach that had been used to characterize the graph analytical features of the two simulated hyperactivity signals also identified a real data cluster consistent with intermittent neuronal hyperactivity, i.e., increased pos and decreased neg strength associated with increased pos diversity indicating an increased interaction between modules or communities. Its graph analytical signature was very similar to that of the unbalanced synchron -type signature observed in the simulated data. The number of windows in subjects showing this synchron -type graph analytical patterns was positively correlated with their SUVR supporting the hypothesized relationship between intermittent neuronal hyperactivity and amyloid load.

As in the simulated data, these hyperactivity epochs in real data were associated with background activity whose graph analytical signature was similar to their own but less prominent. The amount of time during which that background activity occurred was longer in subjects in whom phases of intermittent neuronal hyperactivity were observed than in those in whom that was not the case (with cluster 8 vs. without cluster 8: cluster 7: mean: 27.8 ± 18.2 vs. mean: 11.9 ± 12.1, $p < 0.05$; cluster 6: mean: 16.5 ± 13.1 vs. mean: 9.6 ± 7.6 $p = 0.07$). This could indicate that the background activity preceding the hyperactivity epoch represents not only a transition from normal to abnormal activity but rather a state that has to last for a minimal amount of time for the hypersynchronous signal to be able to generate a detectable imprint.

Only 21 of the 49 subjects showed this intermittent hyperactivity though. One explanation for this could be the same as for the limited detection of the synchron-signal in simulated data, i.e., the limited ability of the global approach to identify a distinct signature of a relatively weak hypersynchronous signal. In this case, it should be possible to increase the likelihood to identify a distinct signature by focusing on brain regions suspected to be most likely involved in the generation of the hyperactivity, e.g. the temporal lobes. Another explanation is that the hypersynchronous hyperactivity responsible for the appearance of this graph analytical activity in a task-free state is indeed a paroxysmal event as suggested by the EEG studies in MCI and AD. In this case, its detectability could be enhanced by increasing the acquisition time. Finally, it cannot be excluded that this type of intermittent hyperactivity occurs indeed only in a particular subset of CN. Longitudinal studies could help to investigate this possibility and its role in the development of AD.

The findings of this study suggest that amyloid can cause widespread, weak intermittent hypersynchrony in cognitively intact older subjects that shared several features with amyloid associated hyperactivity observed in animal models of AD (Stern et al. 2004; Kellner et al. 2014; Shah et al. 2016). For example, similarly as in AD animal models, the hypersynchrony was widespread (Shah et al. 2016). This is probably only possible in the earliest stages of the disease when gray and white matter structures enabling synchronization between distant brain regions are still mostly intact (Mueller and Weiner 2017). Progressive synaptic loss and neuronal dysfunction/loss due to the toxic effects of amyloid are likely to initially "reshape" the hyperactivity, e.g. prevent widespread hypersynchrony but increase the likelihood of focal hypersynchrony and thereby of epileptogenic discharges (Lam et al. 2017). In the long run however, neuronal loss will likely abolish the ability to initiate hyperactivity states and thereby initiate the transition from a state of hyperexcitability to the state of hypoexcitability that characterizes the later stages of AD (Schultz et al. 2017; Demirtaş et al. 2017). Another feature shared with animal models was that short hypersynchrony episodes could already be observed in subjects with normal amyloid load and became longer with increasing amyloid load. This could indicate that oligomeric amyloid is the driving force behind these disturbances and not plaque amyloid. Oligomeric amyloid as the main agent of hypersynchrony would also explain why hypersynchrony duration was significantly associated with memory performance and amyloid load but memory performance and amyloid load were not associated with each other. The negative association between hypersynchrony duration and memory performance in the absence of objective memory impairment suggests that these hypersynchrony episodes have the potential to interfere with cognitive performance if they become more frequent, last longer or are triggered by tasks that engage networks involved in their generation. The latter possibility is supported by the studies of Bakker and co-workers (Bakker et al. 2012, 2015) who demonstrated a task associated hyperactivity in the mesial temporal lobes of MCI subjects performing a pattern separation test. Interestingly, treatment with levetiracetam not only suppressed the hyperactivity but also improved task performance. This could indicate that levetiracetam might eventually also be able to suppress the hypersynchrony episodes observed in this study.

Comparison with other dynamic task-free fMRI approaches

Several intriguing approaches for the dynamic analysis of task-free fMRI have been proposed in recent years, e.g., Jones et al. 2012, Chen et al. 2015, Liu et al. 2013, Zalesky et al. 2014, Allen et al. 2014, Leonardi et al. 2013; Kiviniemi et al. 2011, Hutchison et al. 2013, Yang et al.2014, Betzel et al. 2016; De Vos et al. 2018, Demirtaş et al. 2017, Córdova-Palomera et al. 2017; Wee et al. 2016., Khambhati et al. 2018, please see Preti et al. 2017 for a review). Most focus on connectivity fluctuations within the boundaries of networks originally derived from stationary analyses, on identifying and characterizing a predefined number of network configurations or on fluctuations of the community structure. More importantly though, most of these approaches focus on describing connectivity fluctuations during the same activity state which is rest. In contrast, this study attempts to capture the disruption of the normal task-free activity by a non-physiological intermittent disturbance. In contrast to other dynamic analysis analyses, the approach used here does not necessarily assume that the fluctuations in the absence of this non-physiological disturbance contain indeed meaningful biological information. Furthermore, the approach introduced here uses a global measure of brain connectivity to identify different states of connectedness and thus it is very likely that epochs that have been assigned to the same cluster encompass different network configurations. In summary, the approach proposed here captures different aspects of the brain dynamic than other dynamic approaches which prevents a direct comparison. The fact that so many different approaches for dynamic task-free fMRI analysis have been introduced in the last couple of years indicates that this field generates a lot of interest and promise but is still in its early stages. More research is needed to determine how useful the combined cluster/graph analysis approach introduced here will be for understanding the healthy and diseased brain.

Limitations

This study has several limitations. 1. The size of the study population was small. The next step is to replicate the finding

in another independent data set which was recently done in a small pilot study with 27 randomly selected non-demented ADNI3 subjects (13 CN and 14 MCI, mean age: 71.2 (5.2), mean MMSE: 28.4 (3.0), mean ADAScog: 12.5 (6.2), mean SUVR: 1.08 (0.13), range: 0.87–1.39, amyloid neg: 17, amyloid pos:9). The data was processed in the same way as described in the manuscript. The method described in the manuscript was used compare the graph signature found in the ADNI3 pilot population with those of the population described here and with the cluster signature of the simulated data. The ADNI 3 cluster with the highest dice to the amyloid cluster (dice: 0.73) was also the best match for the simulated "synchron signal" (dice: 0.78). Using correlation analyses, significant positive correlations between the duration of ADNI3 cluster were found for Abeta load ($r = 0.47$, $p = 0.01$ and ADAScog ($r = 0.45$, $p = 0.01$). None of the other clusters identified in the ADNI3 data showed the these associations. 2. The EPI sequence used in this study used a TR of 3 s which is relatively long for a dynamic analysis where shorter TR and thus more timepoints/window are desirable. It cannot be excluded that short intermittent amyloid induced abnormalities were missed because of this. 3. One of the challenges of the sliding windows approach is the choice of the correct window length since a too short window can cause spurious fluctuations and a too long window can smooth physiological fluctuations. A recent study that used simulated BOLD fluctuations to investigate the relationship between window length and spurious fluctuations suggested that the combination of a high-pass filter of 0.008 with a window length of 45 s used in this study could result in spurious fluctuations (Leonardi and Van De Ville 2014). We consider it unlikely though that the findings reported here were caused by spurious fluctuations. Spurious fluctuations caused by too short windows should affect amyloid pos and amyloid neg CN equally (Hutchison et al. 2013; Zalesky and Breakspear 2015) and would not be expected to show a relationship with amyloid load and memory performance. Nonetheless the influence on window length on the graph analytical profiles described in this study needs to be carefully investigated. 4. The study used simulations of two different types of abnormal neuronal firing observed in animal models with increased amyloid levels. Simulating these events requires making assumptions about their behavior based on what is known about them from the literature. These assumptions might not be entirely correct. The conclusions regarding the nature of the amyloid associated abnormalities in the real data based on their similarity to these simulated signals have therefore to be further corroborated. The next step to do this are simultaneous EEG/MRI studies. This will also allow to definitively exclude a contribution of sleepiness to the findings reported here although one would not expect to find an association between amyloid load and the length of the hyperactivity phases if sleepiness were indeed a major contributor.

Conclusion

The dynamic analysis combined with graph analysis detected evidence for intermittent amyloid associated disturbances of the functional connectivity. The results from the simulated data suggests that these disturbances could be caused by those short phases of hypersynchronous activity that have been described in quantitative EEG analyses of AD and MCI patients. The frequency of these disturbances was relatively low and did not affect the cognitive abilities in the study population (please see Table 1). However, given that the length of these episodes was negatively correlated with memory performance it seems likely that these disturbances have the potential to interfere with cognitive processes and could lead to cognitive impairment if they become more frequent or more severe with increasing amyloid deposition. Given the relatively small sample size, these findings have to be considered preliminary and need to be repeated, ideally with simultaneous EEG recordings, in a larger population that also includes cognitively impaired individuals.

Acknowledgements The study was supported by a NIH grant R01 AG010897 (PI Michael Weiner) and a UCSF grant REAC/CTSI 37785-525205 to SGM. SGM would like to thank Dr. Weiner for making his data available. Thanks also to A.M.M for the critical reading of an early draft of the manuscript.

Funding The study was supported by NIH grant R01 AG010897 (PI Michael Weiner) and a UCSF grant REAC/CTSI 37785–525205 to SGM.

Compliance with ethical standards

Conflict of interest The author has no conflict of interest to declare.

Ethical approval This study was done with human participants after obtaining informed consent. All procedures performed in this study were in accordance with the ethical standards of the committees of human research at the University of California, San Francisco (UCSF) and VA Medical Center San Francisco, and with the 1964 Helsinki declaration and its later amendments or comparable ethical standards.

References

Allen, E. A., Damaraju, E., Plis, S. M., Erhardt, E. B., & Eichele, T. (2014). Calhoun V (2014): Tracking whole brain connectivity dynamics in the resting state. *Cerebral Cortex, 24*, 663–676.

An, D., Dubeau, F., & Gotman, J. (2015). BOLD responses related to focal spikes and widespread bilateral synchronous discharges generated in the frontal lobe. *Epilepsia, 56*, 366–374.

Bai, X., Guo, J., Killory, B., Vestal, M., Berman, R., Negishi, M., Danielson, N., Novotny, E. J., Constable, R. T., & Blumenfeld, H. (2011). Resting functional connectivity between the hemispheres in childhood absence epilepsy. *Neurology, 76*, 1960–1967.

Bakker, A., Krauss, G. L., Albert, M. S., Speck, C. L., Jones, L. R., Stark, C. R., Yassa, M. A., Bassett, S. S., Shelton, A. L., & Gallagher, M.

(2012). Reduction of hippocampal hyperactivity improves cognition in amnestic mild cognitive impairment. *Neuron, 74*, 467–474.

Bakker, A., Albert, M. S., Krauss, G., Speck, C. L., & Gallagher, M. (2015). Response of the medial temporal lobe network in amnestic mild cognitive impairment to therapeutic intervention assessed by fMRI and memory task performance. *Neuroimage Clinical, 7*, 688–698.

Betzel, R., Fukushima, M., He, Y., Zuo, X.-N., & Sporns, O. (2016). Dynamic fluctuations coincide with periods of high and low modularity in resting-state functional brain networks. *NeuroImage, 127*, 287–297.

Born, H. A. (2015). Neuroscience forefront review: Seizures in Alzheimer's disease. *Neuroscience, 286*, 251–263.

Brier, M. R., Thomas, J. B., Fagan, A. M., Hassenstab, J., Holtzman, D. M., Benzinger, T. L., Morris, J. C., & Ances, B. M. (2014). Functional connectivity and graph theory in preclinical Alzheimer's disease. *Neurobiology of Aging, 35*, 757–768.

Busche, M. A., Chen, X., Henning, H. A., Reichwald, J., Staufenbiel, M., Sakman, B., & Konnerth, A. (2012). Critical role of soluble amyloid beta for early hippocampal hyperactivity in a mouse model of Alzheimer's disease. *Proceeding of the National Academy of Science, 109*, 8740–8745.

Carbonell, F., Bellec, P., & Shmuel, A. (2014). Quantification of the impact of a confounding variable on functional connectivity confirms anti-correlated networks in the resting state. *NeuroImage, 86*, 343–353.

Chai, X., Nieto Castañon, A., & Öngür, D. (2012). Whitfield-Gabrieli S (2012): Anticorrelations in resting state networks without global signal regressions. *NeuroImage, 59*, 1420–1428.

Chang, C., Liu, Z., Chen, M. C., Liu, X., & Duyn, J. H. (2013). EEG correlates of time-varying BOLD functional connectivity. *NeuroImage, 72*, 227–236.

Chen, J. E., Chang, C., Greicius, M. D., & Glover, G. H. (2015). Introducing co-activation pattern metrics to quantify spontaneous brain network dynamics. *NeuroImage, 111*, 476–488.

Córdova-Palomera, A., Kaufmann, T., Persson, K., Alnæs, D., Doan, N. T., Moberget, T., Lund, M. J., Barca, M. L., Engvig, A., Brækhus, A., Engedal, K., Andreassen, O. A., Selbæk, G., & Westlye, L. T. (2017). Disrupted global metastability and static and dynamic brain connectivity across individuals in the Alzheimer's disease continuum. *Scientific Reports, 7*, 40268.

Demirtaş, M., Falcon, C., Tucholka, A., Gispert, J. D., Molinuevo, J. L., & Deco, G. (2017). A whole-brain computational modeling approach to explain the alterations in resting-state functional connectivity during progression of Alzheimer's disease. *Neuroimage: Clinical, 16*, 343–354.

De Vos F, Koini M, Schouten TM, Seiler S, van der Grond J, Lechner A, Schmidt R, van der Rooj M, Rombouts SARB (2018). A comprehensive analysis of resting state fMRI measures to classify individual patients with Alzheimer's disease. NeuroImage, 167; 62–72.

Erhardt, E. B., Allen, E. A., Wei, Y., Eichele, T., & Calhoun, V. D. (2012). SimTB, a simulation toolbox for fMRI data under a model of spatiotemporal separability. *NeuroImage, 59*, 4160–4167.

Faizo, N. L., Burianova, H., Gray, M., Hicking, J., Galloway, G., & Reutens, R. (2014). Identification of pre-spike network in patients with temporal lobe epilepsy. *Frontiers in Neurology, 5*. https://doi.org/10.3389/fneur.2014.00222.

Grienberger, C., Rochefort, N. L., Adelsberger, H., Henning, H. A., Hill, D. N., Reichwald, J., Staufenbiel, M., & Konnerth, A. (2012). Staged decline of neuronal function in vivo in an animal model of Alzheimer's disease. *Nature Communications, 3*, 774. https://doi.org/10.1038/ncomms1783.

Hutchison, R. M., Wormelsdorf, T., Allen, E. A., Bandettini, P. A., Calhoun, V. D., Corbetta, M., Della Penna, S., Duyn, J. H., Glover, G. H., Gonzalez-Castillo, J., Handwerker, D. A., Keilholz, S., Kiviniemi, V., Leopold, D. A., de Pasquale, F., Sporns, O., Walter, M., & Chang, C. (2013). Dynamic functional connectivity: Promise, issues and interpretations. *NeuroImage, 15, 80*. https://doi.org/10.1016/j.neuroimage.2013.05.079.

Jack, C. R., Wise, H. J., Weigand, S. D., Knopman, D. S., Lowe, V., Vermuri, P., Mielke, M. M., Jones, D. T., Senjem, M. L., Gunter, J. L., Gregg, B. E., Pankratz, V. S., & Petersen, R. C. (2013). Amyloid-first and neurodegeneration-first profiles characterize incident amyloid PET positivity. *Neurology, 81*, 1732–1740.

Joliot, M., Jobard, G., Naveau, M., Delcroix, N., Petit, L., Zago, L., Crivello, F., Mellet, E., Mazoyer, B., & Tzourio-Mazoyer, N. (2015). AICHA: An atlas of intrinsic connectivity of homotopic areas. *Journal of Neuroscience Methods, 254*, 46–59.

Jones, D. T., Vermuri, P., Murphy, M. C., Gunter, J. L., Senjem, M. L., Machulda, M. M., Przybelski, S. A., Gregg, B. E., Kantarci, K., Knopman, D. S., Boeve, B. F., Petersen, R. C., & Jack, C. R. (2012). Non stationarity in "resting brain's" modular architecture. *PLoS One, 7*(6), e39731.

Joshi, A. D., Pontecorvo, M. J., Lu, M., Skovronsky, D. M., Mintun, M. A., & Devous, M. D. (2015). A Semiautomated method for quantification of F 18 Florbetapir PET images. *The Journal of Nuclear Medicine, 56*, 1736–1741.

Kay, B. P., Holland, S. K., Privitera, M. D., & Szaflarski, J. P. (2014). Differences in paracingulate connectivity associated with epileptiform discharges and uncontrolled seizures in genetic generalized epilepsy. *Epilepsia, 55*, 256–263.

Khambhati, A., Mattar, M. G., Wymbs, N. F., Grafton, S. T., & Bassett, D. S. (2018). Beyond modularity: Fine scale mechanisms and rules for brain network reconfigurations. *NeuroImage, 166*, 385–399.

Keller, C. J., Bickel, S., Honey, C. J., Groppe, D. M., Entz, L., Craddock, R. C., Lado, F. A., Kelly, C., Milham, M., & Metha, A. D. (2013). Neurophysiological investigation of spontaneous correlated and anticorrelated fluctuations of the BOLD signal. *The Journal of Neuroscience, 33*, 6333–6342.

Kellner, V., Menkes-Caspi, N., Beker, S., & Stern, E. A. (2014). Amyloid beta alters ongoing neuronal activity and excitability in the frontal cortex. *Neurobiology of Aging, 35*, 1982–1991.

Kiviniemi, V., Vire, T., Remes, J., Elseoud, A. A., Starck, T., & Tervonen, O. (2011). Nikkinen (2011): A sliding window ICA reveals spatial variability of the default mode network in time. *Brain Connectivity, 1*, 339–347.

Kleen, J. K., Scott, R. C., Holmes, G. L., Roberts, D. W., Rundle, M. M., Testorf, M., Lenck-Satini, P. P., & Jobst, B. C. (2013). Hippocampal interictal epileptiform activity disrupts cognition in humans. *Neurology, 81*, 18–24.

Lam, A. D., Deck, G., Goldman, A., Eskandar, E. N., Noebels, J., & Cole, A. J. (2017). Silent hippocampal seizures and spikes identified by foramen ovale electrodes in Alzheimer's disease. *Nature Medicine, 23*, 678–680.

Leonardi, N., Richiardi, J., Gschwind, M., Simioni, S., Annoni, J. M., Schluep, M., Vuilleumier, P., & Van De Ville, D. (2013). Principal components of functional connectivity: A newapproach to study dynamic brain connectivity during rest. *NeuroImage, 83*, 937–950.

Leonardi, N., & Van De Ville, D. (2014). On spurious and real fluctuations of dynamic functional connectivity during rest. *NeuroImage, 104*, 430–436.

Liedorp, M., van der Flier, W. M., Hoogervorst, E. L. J., Scheltens, P., & Stam, C. J. (2009). Associations between patterns of EEG abnormalities and diagnosis in a large memory cohort. *Dementia and Geriatric Cognitive Disorders, 27*, 18–23.

Liedorp, M., Stam, C. J., van der Flier, W. M., Pijnenburg, Y. A., & Scheltens, P. (2010). Prevalence and clinical significance of epileptiform EEG discharges in a large memory clinic cohort. *Dementia and Geriatric Cognitive Disorders, 29*, 432–437.

Lopes, R., Moeller, F., Besson, P., Ogez, F., Szurhaj, W., Leclerc, X., Siniatchkin, M., Chipaux, M., Derambure, P., & Tryvaert, L. (2014). Study on the relationships between intrinsic functional

connectivity of the default mode network and transient epileptic activity. *Frontiers in Neurology, 5*. https://doi.org/10.3389/fneur.2014.00201.

Liu, X., Chang, C., & Duyn, J. H. (2013). Decomposition of spontaneous brain activity into distinct fMRI co-activation patterns. *Frontiers in Systems Neuroscience* Dec 4*, 7*, 101.

Liu, J. V., Kobylarz, J., Darcey, T. M., Lu, Z., Wu, Y. C., Meng, M., & Jobst, B. C. (2014). Improved mapping of interictal epileptiform discharges with EEG-fMRI and voxel-wise functional connectivity analysis. *Epilepsia, 55*, 1380–1388.

Mishra, A. M., Bai, X., Motelow, J. E., DeSalvo, M. N., Danielson, N., Sanganahalli, B. G., Hyder, F., & Blumenfeld, H. (2013). Increased functional connectivity in spike-wave epilepsy in WAG/RJi rats. *Epilepsia, 54*, 1214–1222.

Mueller, S. G., Chao, L. L., Berman, B., & Weiner, M. W. (2011). Evidence for functional specialization of hippocampal subfields detected by MR subfield volumetry on high resolution images at 4T. *NeuroImage, 56*, 851–857.

Mueller, S. G., & Weiner, M. W. (2017). Amyloid associated intermittent network disruptions in cognitively intact older subjects: Structural connectivity matters. *Frontiers in Aging Neuroscience, 9*, 418. https://doi.org/10.3389/fnagi.2017.00418.

Mucke, L., & Selkoe, D. L. (2012). Neurotoxcicity of amyloid beta protein: Synaptic and network dysfunction. *Cold Spring Harbor Perspectives in Medicine* Jul*, 2*(7), a006338. https://doi.org/10.1101/cshperspect.a006338.

Murphy, K., Birn, E. M., Handwerker, D. A., Jones, T. B., & Bandettini, P. A. (2009). The impact of global signal regression on resting state correlations: Are anti-correlated networks introduced? *NeuroImage, 44*, 893–905.

Palop, J. J., Chin, J., Roberson, E. D., Wang, J., Thwin, M. T., Bien-Ly, N., Yoo, J., Ho, K. Q., Yu, G. Q., Kreitzer, A., FInkbeiner, S., Noebels, J. L., & Mucke, L. (2007). Aberrant excitatory neuronal activity and compensatory remodeling of inhibitory hippocampal circuits in mouse models of Alzheimer's disease. *Neuron, 55*, 697–711.

Palop, J. J., & Mucke, L. (2010). Amyloid-beta-induced neuronal dysfunction in Alzheimer's disease: From synapses toward neural networks. *Nature Neuroscience, 13*, 812–818.

Power, J. D., Barnes, K. A., Snyder, A. Z., Schlaggar, B. L., & Petersen, S. E. (2012). Spurious but systematic correlations in functional connectivity arise from subject motion. *NeuroImage, 59*, 2142–2154.

Power, J. D., Mitra, A., Laumann TO, Snyder, A. Z., Schlaggar, B. L., & Petersen, S. E. (2014). Methods to detect, characterize, and remove motion artifacts in resting state fMRI. *NeuroImage, 84*, 320–341.

Power, J. D., Schlaggar, B. L., & Petersen, S. E. (2015). Recent progress and outstanding issues in motion correction in resting state fMRI. *NeuroImage, 105*, 536–551.

Preti, M. G., Bolton, T. A. W., & Van De Ville, D. (2017). The dynamic functional connectome: State of the art and perspectives. *NeuroImage, 160*, 41–54.

Rubinov, M., Sporns, O. (2010). Complex network measures of brain connectivity: uses and interpretations. *NeuroImage, 52*(3):1059–1069.

Rubinov, M., & Sporns, O. (2011). Weight-conserving characterization of complex functional brain networks. *NeuroImage, 56*, 2068–2079.

Sanchez, P. E., Zhu, L., Verret, L., Vossel, K. A., Orr, A. G., Cirrito, J. R., Devidze, N., Ho, K., Yu, G. Q., Palop, J. J., & Mucke, L. (2012). Levetiracetam suppresses neuronal network dysfunction and reverses synaptic and cognitive deficits in an Alzheimer disease model. *Proceedings of the National Academy of Sciences, 109*, 2895–2903.

Schultz, A. P., Chhatwal, J. P., Hedden, T., Mormino, E. C., Henseeuw, B. J., Sepulcre, J., Huijbers, W., La Point, M., Buckley, R. F., Johnson, K. A., & Sperling, R. A. (2017). Phases of hyperconnectivity and hypoconnectivity in the default mode and salience networks track with amyloid and tau in clinically normal individuals. *The Journal of Neuroscience, 37*, 4323–4331.

Shah, D., Praet, J., Latif Hernandez, A., Höfling, C., Anckaerts, C., Bard, F., Morawski, M., Detrez, J. R., Prinsen, E., Villa, A., De Vos, W. H., Maggi, A., D'Hooge, R., Balschun, D., Rossner, S., Verhoye, M., & Van der Linden, A. (2016). Early pathologic amyloid induces hypersynchrony of BOLD resting-state networks in transgenic mice and provides an early therapeutic window before amyloid plaque deposition. *Alzheimers Dement, 12*, 964–976.

Sheline, Y. I., Raichle, M. E., Snyder, A. Z., Morris, J. C., Head, D., Wang, S., & Mintun, M. (2010). Amyloid plaques disrupt resting state default mode network connectivity in cognitively normal elderly. *Biological Psychiatry, 67*, 584–587.

Smailovic, U., Koenig, T., Kåreholt, I., Andersson, T., Kramberger, M. G., Winblad, B., & Jelic, V. (2017). Quantitative EEG power and synchronization correlate with Alzheimer's disease CSF biomarkers. *Neurobiology of Aging, 63*, 88–95.

Smits LL, Liedorp M, Koene T, Roos-Reuling IE, Lemstra AW, Scheltens P, Stam CJ, van der Flier WM (2011): EEG abnormalities are associated with different cognitive profiles in Alzheimer's disease. Dementia and Geriatric Cognitive Disorders 31: 1–6.

Sperling, R. A., LaViolette, P. S., O'Keefe, K., O'Brien, J., Rentz, D. M., Pihlajamaki, M., Marshall, G., Hyman, B. T., Selkoe, D. J., Hedden, T., Buckner, R. L., Becker, J. A., & Johnson, K. A. (2009). Amyloid deposition is associated with impaired default network function in older persons without dementia. *Neuron, 63*, 178–188.

Sporns, O., Tononi, G., & Edelman, G. M. (2000). Theoretical neuroanatomy: Relating anatomical and functional connectivity in graphs and cortical connection matrices. *Cerebral Cortex, 10*, 127–141.

Stargardt, A., Swaab, D. F., & Bossers, K. (2015). The storm before the quiet: Neuronal hyperactivity and Abeta in the presymptomatic stages of Alzheimer's disease. *Neurobiology of Aging, 36*, 1–11.

Steininger, S. C., Liu, X., Gietl, A., Wyss, M., Schreiner, S., Gruber, E., Treyer, V., Kälin, A., Leh, S., Buck, A., Nitsch, R. M., Pruessmann, K. P., Hock, C., & Unschud, P. G. (2014). Cortical amyloid beta in cognitively normal elderly adults is associated with decreased network efficiency within the cerebro-cerebellar system. *Frontiers in Aging Neuroscience* 18*, 6*, 52. https://doi.org/10.3389/fnagi.2014.0052 eCollection 2014.

Stern, E. A., Bacskai, B. J., Hickey, G. A., Attenello, F. J., Lombardo, J. A., & Hyman, B. T. (2004). Cortical synaptic integration in vivo is disrupted by amyloid plaques. *The Journal of Neuroscience, 24*, 4535–4540.

Stomrud, E., Hansson, O., Minthon, L., Blennow, K., Rosén, I., & Londos, E. (2010). Slowing of EEG correlates with CSF biomarkers and reduced cognitive speed in elderly with normal cognition over 4 years. *Neurobiology of Aging, 31*, 215–223.

Talantova, M., Sanz-Blasco, S., Zhang, X., Xia, P., Akhtar, M. W., Okamoto, S. I., Dziewczapolski, G., Nakamura, T., Cao, G., Pratt, A. E., Kang, Y. J., Tu, S., Molokanova, E., McKercher, S. R., Hires, S. A., Sason, H., Stouffer, D. G., Buczynski, M. W., Solomon, J. P., Michael, S., Powers, E. T., Kelly, J. W., Roberts, A., Tong, G., Fang-Newmeyer, T., Parker, J., Holland, E. A., Zhang, D., Nakanishi, N., Chen, H. S. V., Wolosker, H., Wang, Y., Parsons, L. H., Ambasudhan, R., Masliah, E., Heinemann, S. F., Pina-Crespo, J. C., & Lipton, S. A. (2013). Abeta induces astrocytic glutamate release, extrasynaptic NMDA receptor activation and synaptic loss. *Proceedings of the National Academy of Sciences, 110*, 2518–2527.

Vossel, K. A., Beagle, A. J., Rabinovici, G. D., Shu, H., Lee, S. E., Naasan, G., Hegde, M., Cornes, S. B., Henry, M. L., Nelson, A. B., Seeley, W. W., Geschwind, M. D., Gorno-Tempini, M. L., Shih, T., Kirsch, H. E., Garcia, P. A., Miller, B. L., & Mucke, L. (2013). Seizures and epilepptiform activity in the early stages of Alzheimer's disease. *JAMA Neurology, 70*, 1158–1166.

Vossel, K. A., Ranasinghe, K. G., Beagle, A. J., Mizuiri, D., Honma, S. M., Dowling, A. F., Darwish, S. M., Van Berlo, V., Barnes, D. E.,

Mantle, M., Karydas, A. M., Coppola, G., Roberson, E. D., Miller, B. L., Garcia, P. A., Kirsch, H. E., Mucke, L., & Nagarajan, S. S. (2016). Incidence and impact of subclinical epileptiform activity in Alzheimer's disease. *Annals of Neurology, 80*, 858–870.

Wang, L., Brier, M. R., Snyder, A. Z., Thomas, J. B., Fagan, A. M., Xiong, C., Benzinger, T. L., Holtzman, D. M., Morris, J. C., & Ances, B. M. (2013). Cerebrospinal fluid Abeta42, phosphorylates Tau181, and resting-state functional connectivity. *JAMA Neurology, 70*, 1242–1248.

Wee, C. Y., Yang, S., Yap, P. T., & Shen, D. (2016). Sparse temporally dynamic resting-state functional connectivity networks for early MCI identification. *Brain Imaging and Behavior, 10*, 342–356.

Wennberg, R., Valiante, T., & Cheyne, D. (2011). EEG and MEG in mesial temporal lobe epilepsy. Where do the spikes really come from? *Clinical Neurophysiology, 122*, 1295–1313.

Whitfield-Gabrieli, S., & Nieto-Castagnon, A. (2012). Conn a functional connectivity toolbox and anticorrelated brain networks. *Brain Connectivity, 2*, 125–141.

Yang, Z., Craddock, R. C., Margulies, D. S., Yan, C. G., & Milham, M. P. (2014). Common intrinsic connectivity states among posteromedial cortex subdivisions: Insights from the analysis of temporal dynamics. *NeuroImage, 93*, 124–137.

Zalesky, A., Fornito, A., Cocchi, L., Gollo, L. L., & Breakspear, M. (2014). Time resolved resting-state networks. *Proceedings of the National Academy of Sciences, 111*, 1034–10346.

Zalesky A, Breakspear M (2015): Towards a statistical test for functional connectivity dynamics. Neuroimage. https://doi.org/10.11016/j.neuroimage.2015.03.047